Processes and mechanisms in remediation of aqueous chromium contamination by sulfidated nano-scale zerovalent iron (S-nZVI): Experimental and computational investigations

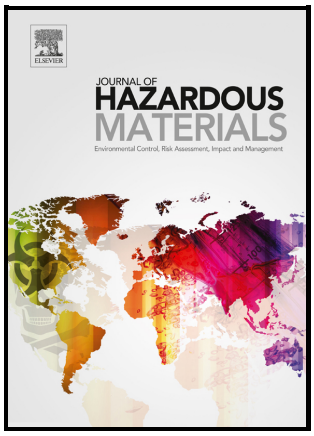

Yuanyuan Wang, Yuesuo Yang, Jinyu Shi, Wengang An, Tao Lyu, Ping Zhang

PII: S0304-3894(24)00610-1

DOI: https://doi.org/10.1016/j.jhazmat.2024.134031

Reference: HAZMAT134031

To appear in: *Journal of Hazardous Materials*

Received date: 27 January 2024
Revised date: 8 March 2024
Accepted date: 12 March 2024

Please cite this article as: Yuanyuan Wang, Yuesuo Yang, Jinyu Shi, Wengang An, Tao Lyu and Ping Zhang, Processes and mechanisms in remediation of aqueous chromium contamination by sulfidated nano-scale zerovalent iron (S-nZVI): Experimental and computational investigations, *Journal of Hazardous Materials,* (2024) doi:https://doi.org/10.1016/j.jhazmat.2024.134031

Journal of Hazardous Materials, Volume 469, May 2024, Article Number 134031
DOI: 10.1016/j.jhazmat.2024.134031

Processes and mechanisms in remediation of aqueous chromium contamination by sulfidated nano-scale zerovalent iron (S-nZVI): Experimental and computational investigations

Yuanyuan Wang[a], Yuesuo Yang[b*], Jinyu Shi[b], Wengang An[b], Tao Lyu[c], Ping Zhang[a*]

[a] *Department of Civil and Environmental Engineering, Faculty of Science and Technology, University of Macau, Taipa, Macau*

[b] *Key Lab of Groundwater Resources and Environment, Ministry of Education, Jilin University, Changchun, 130021, China*

[c] *School of Water, Energy and Environment, Cranfield University, College Road, Cranfield, Bedfordshire MK43 0AL, UK*

Corresponding author: * yangyuesuo@jlu.edu.cn (Y.S. Yang), * pzhang@um.edu.mo (P. Zhang)

Abstract

Sulfidated nano-scale zerovalent iron (S-nZVI) has emerged as an advanced functional nanomaterial for efficiently remediating Cr(VI) contamination in aqueous environments. However, there is an insufficient understanding of its coherent process, removal pathway, and hydrochemical reactive mechanisms, presenting potential challenges for its future environmental applications. To address this gap, this study successfully synthesized S-nZVI through a chemical precipitation method and effectively applied it for the removal of Cr(VI). Additional characterization revealed that the removal of Cr(VI) followed a sequence of rapid chemisorption and intraparticle diffusion processes, concomitant with an increase in pH and a decrease in oxidation-reduction potential. The

remediation mechanism encompassed a synergistic reduction of Cr(VI) to Cr(III) and simultaneous immobilization via Cr_2FeO_4 coprecipitation. The highest Cr(VI) removal capacity of 75 mg/g was attained during dynamic removal experiments in the sand column packed with S-nZVI. Further computational analysis, employing density functional theory calculations based on the experimental data, revealed the involvement of multiple molecular orbitals of Cr(VI) in the removal process. It also elucidated a step-by-step reduction pathway for Cr(VI) characterized by decreasing free energy. These findings provide evidence-based insights into Cr(VI) remediation using S-nZVI and can serve as valuable technical support for future environmental management of heavy metals.

Keywords: S-nZVI; chromium; adsorption; co-precipitation; DFT computation

Environmental Implication

Chromium (Cr) is frequently detected in surface water and groundwater, raising potential public health concerns. Sulfidated nano-scale zerovalent iron (S-nZVI) has emerged as an advanced functional nanomaterial for efficiently remediating Cr(VI) contamination. However, there is an insufficient understanding of processes and underlying mechanisms in remediation of aqueous Cr contamination by S-nZVI. This study conducted a comprehensive investigation to understand the processes and mechanisms responsible for Cr(VI) removal by S-nZVI through experimental and computational methods. This study aims to provide evidence-based insights into Cr(VI) remediation using S-nZVI and to serve as valuable technical support for future environmental management of heavy metals.

1. Introduction

The aqueous environment is facing severe pollution due to heavy metals, primarily because numerous industries discharge effluents containing these metals into natural water bodies without adequate treatment (Jin et al., 2018). The presence of toxic heavy metals, including lead (Pb), cadmium (Cd), and chromium (Cr), has raised significant public health concerns. Even at trace concentrations, these metal materials exhibit teratogenic and carcinogenic properties (Su et al., 2019; Wang et al., 2019). Among these, Cr has become a major concern due to its widespread use in electroplating, leather tanning, steel manufacturing, and other industries (Jin et al., 2018; N. Xafenias et al., 2015). For instance, basic chromium sulfate is widely used as a tanning agent, leading to wastewater with Cr concentrations ranging from 500 to 3000 mg/L in Dhaka, Bangladesh(Alam et al., 2020), which is exceedingly higher than WHO permissible discharge limit for Cr of 0.1 mg/L (Nazir et al., 2015). Moreover, Cr generally exhibits a greater mobility compared to Cd, Ni, and Pb, making it more likely to pose a threat to the water environment (Dong et al., 2009; Sherene, 2010). The two predominant oxidation states of Cr, namely Cr(III) and Cr(VI), significantly differ in their environmental mobility and toxicity. Cr(III) demonstrates toxicity 500-1000 times lower than Cr(VI) and readily precipitate due to its affinity to mineral surfaces (Brumovský et al., 2021; Zhang et al., 2013). In contrast, soluble Cr(VI) typically exists in various anionic forms such as $HCrO_4^-$, CrO_4^{2-}, and/or $Cr_2O_7^{2-}$ (Song et al., 2021), with a relatively long residence time ranging from 4.6 to 18 years (Wise Sr et al., 2009). Therefore, the development of low-cost, highly efficient, and environmentally friendly materials and technologies for Cr(VI) remediation is of paramount

importance in ensuring the safety and quality of freshwater, safeguarding public health, and promoting environmental sustainability.

Given the distinct characteristics of Cr(VI) and Cr(III), the concurrent or sequential reduction of Cr(VI) and the immobilization of Cr(III)-containing precipitates are considered a superior remediation strategy (Brumovský et al., 2021). Thanks to advances in materials science, zero-valent iron nanoparticles (nZVIs) and their derived materials have been developed and utilized to efficiently eliminate Cr from contaminated waters (Dong et al., 2017; Huang et al., 2022; Sun et al., 2022; Zhou et al., 2023). For instance, Cr(VI) in groundwater can be removed by using biochar supported green synthetic nZVI-copper or by employing nZVI synthesized with Ginkgo biloba extracts (Li et al., 2024; Li et al., 2022). However, previous studies have identified several challenges hindering the broader environmental applications of nZVI-based materials. The reactivity of nZVI can be substantially reduced due to the formation of a passivation film of iron oxide on the surface of the Fe(0) core (Guan et al., 2015; Yirsaw et al., 2016). Furthermore, the unavoidable reaction of nZVI with water ($Fe^0 + 2H_2O \rightarrow Fe^{2+} + 2OH^- + H_2$) can occur, resulting in a reduced utilization ratio and lifespan of nZVI (Liu and Lowry, 2006).

Sulfidated nano-scale zero-valent iron (S-nZVI) has been recently developed and has demonstrated exceptional removal performance not only for heavy metals such as Pb, Cr, and Cd but also for various other organic pollutants (Han and Yan, 2016; Luo et al., 2014; Lv et al., 2019a; Lv et al., 2018; Zhu et al., 2024). With an active FeS layer coating the nZVI nucleus, S-nZVI can effectively mitigate the formation of passivation layers made of iron oxide (Bhattacharjee and Ghoshal, 2018) and reduce its reactivity with water and other non-target hydrophilic pollutants (e.g., NO_3^-) (Cao et al., 2017; Xu et al., 2019a). Additionally, the presence of FeS_x on the surface of S-nZVI facilitates electron

transfer from the Fe(0) core to Cr(VI) (Lv et al., 2019a). Previous studies have shown that the removal kinetics of Cr(VI) by S-nZVI adhere to the pseudo-second-order model, with the removal process reaching equilibrium within 1-3 hours at initial concentrations of up to 40 mg/L (Brumovský et al., 2021; Li et al., 2018). However, in typical Cr-contaminated water or groundwater near industrial sites, the Cr(VI) concentration can reach as high as 107 mg/L (Zhang et al., 2010). The efficiency, kinetics, and underlying mechanisms of Cr(VI) removal by S-nZVI under environmentally relevant concentrations of Cr(VI) have yet to be substantiated. Furthermore, it is important to recognize that substantial changes in solution pH and oxidation-reduction potential (ORP) can occur during the remediation of Cr(VI) by S-nZVI (Li et al., 2018). Since the distribution and transformation of iron are primarily influenced by the redox environment (Zhang et al., 2021), these changes in hydrochemical conditions, coupled with the reactions, can have a significant impact on the removal performance and environmental risk. This influence extends to the precipitation and dissolution behavior of Cr(VI) at the solid-liquid interface (Zhang et al., 2019a). Therefore, understanding the dynamic interactions between the process of Cr(VI) remediation by S-nZVI and the changes of hydrochemical conditions in the solution is crucial for refining remediation strategies and environmental applications.

The specific application of nZVI and S-nZVI, such as permeable reactive barriers (PRBs) and targeted injection into contaminated aquifers, can date back to the 1990s (Garcia et al., 2021). For instance, a small-scale field test was commenced in September 1994 to assess the in-situ remediation of Cr(VI)-contaminated groundwater (Puls et al., 1999). The remediation method involved employing a PRB composed of a mixture of ZVI, sand, and aquifer sediment. The field site chosen for this study was an abandoned Cr-plating facility located on a U.S. Coast Guard air

base near Elizabeth City, North Carolina. During the remediation process, the dissolved Cr(VI) concentrations in the groundwater were effectively reduced to levels below 0.01 mg/L. This reduction was achieved by converting Cr(VI) to Cr(III) through the corrosion of Fe^0 within the PRB. In another study, researchers introduced core-shell S-nZVI particles into an aquifer previously contaminated with Cr(VI) at a former chrome plating facility (Brumovský et al., 2021). These particles migrated effectively towards the monitoring wells, resulting in a rapid reduction in both Cr(VI) and total Cr concentrations. Moreover, these authors observed a sustained decrease in the redox potential of the groundwater, even at a distance of 35 meters downstream from the nearest injection point. Although this study demonstrates the effectiveness of utilizing S-nZVI to remediate aquifers contaminated with Cr(VI), further investigation is needed to elucidate the detailed interaction mechanism between S-nZVI and Cr(VI), as mentioned above.

To address these research gaps, we conducted a thorough investigation into the mechanisms involved in the reduction and immobilization of Cr(VI) by S-nZVI. This investigation encompassed both experimental studies and molecular-level stoichiometric computations. In this study, both batch and column experiments were carried out to initially evaluate the efficiency of Cr(VI) removal by S-nZVI, which was synthesized using a chemical precipitation method. Subsequently, we identified the dynamic interactions between changes in hydrochemical conditions, including variations in pH and ORP, and the process of Cr(VI) removal. Furthermore, the reduction pathways of Cr(VI) removed by S-nZVI were investigated, employing a combination of experimental approaches and density-functional theory (DFT) calculations. The findings and analyses from this research will serve to facilitate effective engineering implementation of S-nZVI

for remediating heavy metals in aqueous environments and enhancing environmental management of heavy metals.

2. Materials and methods

2.1. Materials and chemicals

All the reagents used in this research, including sodium borohydride ($NaBH_4$, 99%), ferric chloride ($FeCl_3$•$6H_2O$, 99%), sodium sulfide (Na_2S•$9H_2O$, 98%), potassium dichromate ($K_2Cr_2O_7$, 99.5%), and sodium chloride (NaCl, 99.5%), were of analytical grade and were procured from Jinhui Technology Co., Ltd. (Shenyang, China). Deionized water was generated using the Milli-Q system and was employed for all solutions throughout this study. The quartz sand was purchased from Jinhui Technology Co., Ltd. (Shenyang, China) with a particle size ranging from 0.18-0.42 mm. The quartz sand is classified as fine sand with a silica content exceeding 99%.

2.2. Synthesis of S-nZVI

A two-step method was used to synthesize S-nZVI according to the previous studies (Kim et al., 2011; Rajajayavel and Ghoshal, 2015). Briefly, 200 mL of $NaBH_4$ (34 g/L) solution was dropwise added to $FeCl_3$•$6H_2O$ solution (dissolve 9.73 g solid into 200 mL deionized water) with continuously mixing at a rate of 5 mL/min. The whole process was continuously stirred at 600 rpm under the protection of nitrogen gas to form an nZVI suspension. After stirring for extra 20 mins, the solids were separated by a magnet and then washed three times with deoxygenated deionized water. Subsequently, 100 mL of Na_2S (0.18 mol/L) solution was added to the prepared nZVI suspension. After 1 hour, the solids were separated and washed three times using a mixture of 50 mL of deoxygenated deionized water and 50 mL of absolute ethyl alcohol. Finally, the particles were placed in a vacuum-drying oven at 60°C for 8 hours. The dried solids were then gently

grounded into a powder in an agate mortar, poured into a plastic vial as soon as possible to avoid prolonged contact with air, screwed tightly and eventually collected in a desiccator for storage.

2.3. Batch experiments

The Cr(VI) removal efficiency by S-nZVI was first investigated in several batch experiments with the initial concentrations of Cr(VI) of 10, 30, 50, and 100 mg/L in order to simulate different levels of contamination found in real polluted water (Zhang et al., 2010). The batch experimental setup is shown in Fig. S1a. All batch experiments were conducted at room temperature, with each vial sealed and containing approximately 1 mL of headspace. The dose of S-nZVI for all batch experiments was set to be 0.25 g/L, and the initial pH and ORP values were 5.5±0.4 and 300±50 mV, respectively. All the vials were shaken at 120 rpm. Water samples were collected under various reaction time intervals from 0 to 144 h for analysis after being filltered through a 0.22 μm membrane. In order to verify the feasibility and applicability of S-nZVI in practical applications, five Cr(VI)-contaminated groundwater samples (#1, #2, #3, #4, #5) were collected from a contaminated site in Henan province, China. Water chemistry information of these groundwater samples is presented in Table S1.

2.4. Column tests

In order to explore the dynamic remediation of Cr(VI) by S-nZVI materials, the column experiments were conducted in polymethyl methacrylate columns packed with mixed quartz sand and S-nZVI materials to simulate the breakthrough features in the aquifer system (Fig. S1b). The column was 1.0 cm in diameter and 10 cm in length with top and bottom fittings. The quartz sand and S-nZVI materials were mixed with a mass rate of 200:1 and then packed into different columns at an indoor temperature (25±1°C), resulting in total packing materials of 2, 4, 6, and 8 g,

respectively. One more column was used as control, which was filled exclusively with quartz sand. The sand column was placed vertically and the Cr(VI) solution was fed continuously into the columns in an up-flow manner by peristaltic pumps at a flow rate of 0.4 mL/min. For each column, a background electrolyte solution (10 mmol/L NaCl) with pH of approximately 7.0 was first pumped through the column upward for stabilisation. Subsequently, the Cr(VI) solution with a concentration of 50 mg/L was introduced continuously to the packed column with the same pumping rate of 0.4 mL/min. The initial pH of the above Cr(VI) solution was 5.5±0.4 without further adjustment, and all column experiments were conducted at an indoor temperature of 25±1°C. Approximately 2 mL sample from the effluent was collected at suitable intervals and filtered through a 0.22 μm filter for immediate analysis of Cr(VI) concentration. At the end of the column study, the filled packing materials were collected immediately followed by freeze-dried.

2.5. Analytical methods

During the batch experiments, the concentration of Cr(VI) and Fe^{2+} in the collected samples were analyzed by the 1,5-diphenylcarbazide method and phenanthroline spectrophotometry with a UV-visible spectrophotometer (UV-1900, Shimadzu, Japan), respectively. The ORP and pH values were measured by the multi-parameter controller probes (HQ-40D, Hach, U.S.). The models of dynamics and adsorption isotherm of Cr(VI) removal by S-nZVI were shown in Text S1 (Supporting information). The S-nZVI materials were characterized before and after reaction with Cr(VI). The morphological characteristics of the materials were measured by a transmission electron microscope (TEM, Tecnai G2 F30 S-TWIN, U.S.) coupled with energy dispersive spectrometer (EDS). The crystal structures and mineral compositions of S-nZVI materials were analysed by X-ray powder diffraction (XRD, D8 ADVANCE, Germany). The surface chemical composition and chemical state of the S-nZVI were recorded using X-ray photoelectron

spectrometry (XPS, ESCALAB 250 Xi, Thermo Fisher Scientific, U.K.). Following the column experiments, the packing materials were characterized using a scanning electron microscope (SEM) (ZEISS Merlin, Germany) equipped with an energy-dispersive X-ray (EDX) spectrometer.

2.6. Stoichiometric DFT computations

To understand the molecular dynamics of the heavy metal reactions with S-nZVI, the stoichiometry theoretical computations were performed based upon the periodic DFT within the Vienna Ab initio Simulation Package (VASP) (Yang et al., 2023). The general gradient approximation of Perdew-Burke Ernzerdof was adopted for the exchange-correlation functional. The projector augmented wave method was utilized to illustrate the electron-core interactions with a kinetic energy cut-off of 500 eV. Brillouin zones were sampled with a grid of 2 × 2 × 1 Gamma special k-point for the 2 × 2 × 1 FeS supercell. Grimme D3 method was used in dispersion correction for describing weak interaction. The calculation systems were established with periodic boundary conditions. The geometry optimization was stopped when the forces on all unconstrained atoms were less than 0.01 $eV \cdot Å^{-1}$.

3. Results and discussion

3.1. Adsorption on S-nZVI

3.1.1 Adsorptive kinetics of Cr(VI) removal

In this study, the synthesized S-nZVI exhibited a considerable Cr(VI) adsorption capacity of over 110 mg/g. This represented a 1.4 times higher removal efficiency for Cr(VI) compared to conventional nZVI, as illustrated in Fig. S2. These results align with findings from previous research that the equilibrium adsorption capacity of Cr(VI) by nZVI via pseudo-second-order

kinetic was 20.2 mg/g, while S-nZVI with a S/Fe molar ratio of 0.5 was 53.2 mg/g (Lv et al., 2019a). The SEM images of nZVI and S-nZVI are presented in Fig. S3. It shows that nZVI particles tend to aggregate into spherical formations, while S-nZVI forms a chain structure. Moreover, the zeta potential for nZVI and S-nZVI was measured and the pH_{pzc} was calculated to be 8.09 and 8.15, respectively. The difference between these two materials suggests that S-nZVI possesses a slightly higher isoelectric point compared to nZVI. This characteristic enhances the adsorption performance of S-nZVI for negative oxyanions (e.g., $Cr_2O_7^{2-}$) through electrostatic attraction (Tian et al., 2023). In addition, the effect of three different S/Fe ratios (0.1, 0.2, 0.5) on Cr(VI) removal by S-nZVI was shown in Fig. S4, indicating that the S-nZVI with a S/Fe ratio of 0.5 exhibits the best removal ability for Cr(VI) over the lower S/Fe ratios in this experiment. Therefore, the S-nZVI with a S/Fe ratio of 0.5 was selected for Cr(VI) removal in all the other experiments in this study. The detailed adsorption kinetics experiment was initially conducted at an initial pH of 5.5 ± 0.4 without any pH adjustment. The process of Cr(VI) removal by S-nZVI exhibited a two-stage behaviour, as shown in Fig. 1. This included a rapid removal stage within the first 24 hours, followed by a slower equilibrium stage extending up to 144 hours. This behaviour was observed across various initial Cr(VI) concentrations, including 10, 30, 50, and 100 mg/L. Most Cr(VI) was removed by S-nZVI at the first removal stage. Within the first 24 hours, the removal amount of Cr(VI) accounted for over 70% of the total Cr(VI) removal within 144 hours. To analyze the kinetics of this adsorption process, both the pseudo-first order and pseudo-second order models were applied to fit the data, as depicted in Fig. 1a and Fig. 1b and summarized in Table S2. The results indicated that the removal of Cr(VI) was better described by the pseudo-second order kinetic model (R^2>0.991). In fact, the pseudo-second order kinetic results obtained in this study align with the earlier research on Cr(VI) removal using different adsorbing materials (Bhattacharya et al., 2008;

Hossain et al., 2005; Pérez-Candela et al., 1995; Periasamy et al., 1991). These findings suggest that the Cr(VI) removal process is predominantly governed by chemisorption, rather than physical interactions (Hüffer et al., 2013; Luo et al., 2018). In addition, taking into account the electrostatic interaction, the initial rapid adsorption rate can be attributed to the positively charged surface of the S-nZVI particles (with a zeta potential of positive 2.1 mV at initial experimental condition of pH$\approx$6), facilitating the adsorption of anionic Cr(VI) species in the solution. Conversely, the subsequent slower adsorption rate on the curve may arise from electrostatic hindrance induced by previously adsorbed negatively charged species and the gradual pore diffusion of ions (Goswami and Ghosh, 2005; Pandey et al., 2010).

Furthermore, the intraparticle diffusion model was employed to assess the steps involved in Cr diffusion during the adsorption process, as illustrated in Fig. 1c and detailed in Table S2. It is evident that the adsorption process of Cr(VI) by S-nZVI at various initial Cr(VI) concentrations is not linear over the entire reaction duration. This suggests the involvement of multiple mechanisms in governing the adsorption process of Cr(VI) (Bhattacharya et al., 2008). Previous researchers have also observed similar non-linear trends in this form of adsorption behavior (Hossain et al., 2005; Mohanty et al., 2005). The results revealed that the single intraparticle diffusion model yielded high diffusion constants (*C* values ranging from 7.3 to 22.8) and relatively low coefficients (ranging from 0.62 to 0.89). This suggests that intraparticle diffusion was not the sole controlling step in the overall Cr(VI) adsorption process (Su et al., 2020). However, considering the two distinct removal stages observed in the fast and slow removal processes, two separate linear plots with significantly different slopes were apparent for all treatments with varying initial Cr(VI) concentrations, as shown in Fig. 1d. These results imply that two distinct diffusion processes were involved in the

adsorption of Cr(VI). The first stage, characterized by a steep slope, is likely attributed to rapid bulk diffusion or external adsorption. During this stage, approximately 87%, 67%, 53% and 36% of Cr(VI) was removed by S-nZVI when the initial concentrations of Cr(VI) were 10, 30, 50 and 100 mg/L, respectively. The second stage, characterized by a gentler slope, can be attributed to intraparticle diffusion. During this stage, the concentration of Cr(VI) slowly decreased and eventually reached equilibrium, indicating a potentially rate-liming step (Lv et al., 2019b; Su et al., 2020). It is important to note that the fitting curves in Fig. 1c did not pass through the origin, suggesting the complexity of the Cr(VI) adsorption mechanism. Both surface adsorption and intra-particle diffusion likely contribute to determining the reaction rate (Hossain et al., 2005; Mohanty et al., 2005). In addition, the chemical interactions and boundary layer effects also likely played a role in influencing Cr(VI) removal, similar to the removal of Sr^{2+} by a robust layered metal sulfide and Cd (II) by nano-scale molybdenum disulphide sheets in previous studies (Wang et al., 2018; Zhang et al., 2019b).

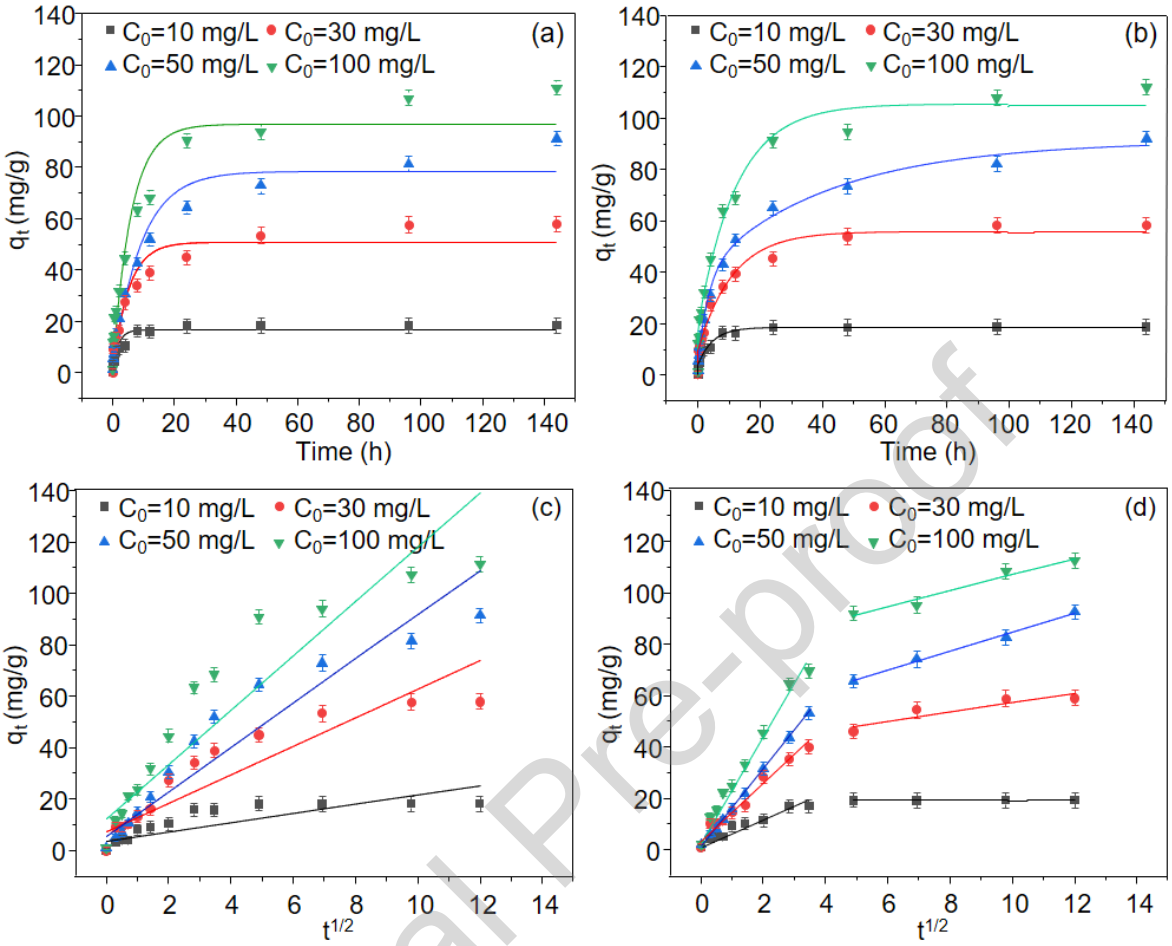

Fig. 1. Kinetics adsorption models of Cr(VI) removed by S-nZVI. (a) Pseudo-first-order kinetic model. (b) Pseudo-second-order kinetic model. (c) Intra-particle diffusion model, and (d) Intraparticle diffusion model of two-section. (S-nZVI=0.25 g/L, solution volume = 20 mL, equilibrium time = 144 h).

3.1.2 Effect of initial Cr (VI) concentration

Both the Langmuir and Freundlich isothermal adsorption models were utilized to simulate the experimental data and assess the adsorption capabilities of S-nZVI, as illustrated in Fig. S5. The analysis revealed that the Langmuir isotherm model provided a more accurate fit compared to the Freundlich model, indicating the potential for monolayer adsorption behaviour (Shen et al., 2013).

The maximum adsorption capacity, calculated using the Langmuir model, was approximately 112.4 mg/g. Using the least square method, the calculated initial adsorption rates (v_0) for different initial concentrations of Cr(VI) (10, 30, 50, and 100 mg/L) were determined to be 15.3, 16.3, 15.2, and 26.8 mg/(g·min), respectively. This data suggested a possible positive correlation between v_0 and the initial Cr(VI) concentration. Theoretically, it is understood that 3 moles of electrons (e^-) are required for the reduction of 1 mole of Cr(VI) to Cr(III). It was estimated that 0.25 g/L of S-nZVI (approximately 4.2 mM) should be sufficient to completely reduce 100 mg/L of Cr(VI) (1.92 mmol/L). This estimation assumes that 1 mole of Fe^0 produces 2 moles of electrons (e^-) to generate Fe^{2+} (Lv et al., 2019a). However, in practice, the removal rate achieved was only 58.8%, which is lower than the theoretical value for 100 mg/L of Cr(VI). These findings suggest that Cr(III)/Fe(III) oxides/hydroxides formed a passivation layer that covered the surface of the S-nZVI material. This passivation layer interfered with the electron transfer from the inner Fe(0) to Cr(VI) and inhibited the reaction process of Cr(VI) removal by S-nZVI (Alidokht et al., 2011). In addition, while it has been pointed out that sulfurization modification can notably attenuate the reaction between nZVI and water molecules (Xu et al., 2019b), it is undeniable that a minor portion of S-nZVI material may diminish the electron utilization ratio in the reduction of Cr(VI) due to its reaction with water molecules. Moreover, the complicated chemical composition of real-world water can influence the removal of heavy metal by S-nZVI (Zheng et al., 2023). The removal efficiency of Cr(VI) by S-nZVI in real groundwater is illustrated in Fig. S6. Following the reaction with S-nZVI, all Cr(VI) concentrations in the real groundwater decreased to below 0.5 mg/L when the initial Cr(VI) concentrations ranged from 5.4 to 15.2 mg/L. This suggests that S-nZVI materials possess the capability to remediate of Cr(VI)-contaminated groundwater.

3.1.3 Characteristics of S-nZVI

The original, pristine S-nZVI particles, before reaction with Cr(VI), exhibited a chain-like structure as shown in Fig. S7. These particles were composed of spherical particles with a relatively smooth surface. However, as the treatment progressed, lamellar and acicular-like particles began to emerge on the surface of the S-nZVI. The lamellar or acicular-like phase that developed on S-nZVI surface was identified as mackinawite, primarily composed of FeS (Fan et al., 2013). This observation suggests that sulfur was successfully loaded onto the surface of the nZVI particles, leading to the formation of S-nZVI. Furthermore, the particle size of the S-nZVI materials experienced a slight increase from 50 nm to 100 nm after reaction with Cr(VI). This size increase can be attributed to the deposition of the reduction product of Cr(VI) onto the surface of the S-nZVI particles. In the XRD patterns of Fig. 2a, a main broad peak at $2\theta=44.6°$ as the evidence of the presence of Fe^0 was clearly observed in the untreated S-nZVI. The small peak at $2\theta=64.5°$ indicated the presence of FeS, suggesting that FeS had been synthesized during the sulfide modification. Specifically, the characteristic peak of FeS was weak due to the low content and poor crystallinity of FeS (Gong et al., 2017). Peaks corresponding to ferrosoferric oxide (Fe_3O_4) and hematite (Fe_2O_3) aligned with the multiple crystallinities of S-nZVI after reaction with Cr(VI). Compared with pristine S-nZVI, the peak of Fe^0 was weakened, the peak of FeS disappeared, and new peaks appeared at $2\theta=35.5°$ (Cr_2FeO_4) and $2\theta=62.7°$ (iron oxides) (Lv et al., 2019a), indicating a redox reaction occurred between S-nZVI and Cr(VI). Moreover, XPS analysis (Fig. 2b) supported the observation of the typical peak Cr 2p in the used S-nZVI, indicating the successful capture of Cr(VI) by S-nZVI material. The atomic percentage of S was considerably reduced from 3.8% to 1.7% along with the increased Cr content (from 0% to 29.3%) during the treatment process (Fig. S8a), and the low S content might be the reason why the S 2p was not observed after the reaction with Cr(VI).

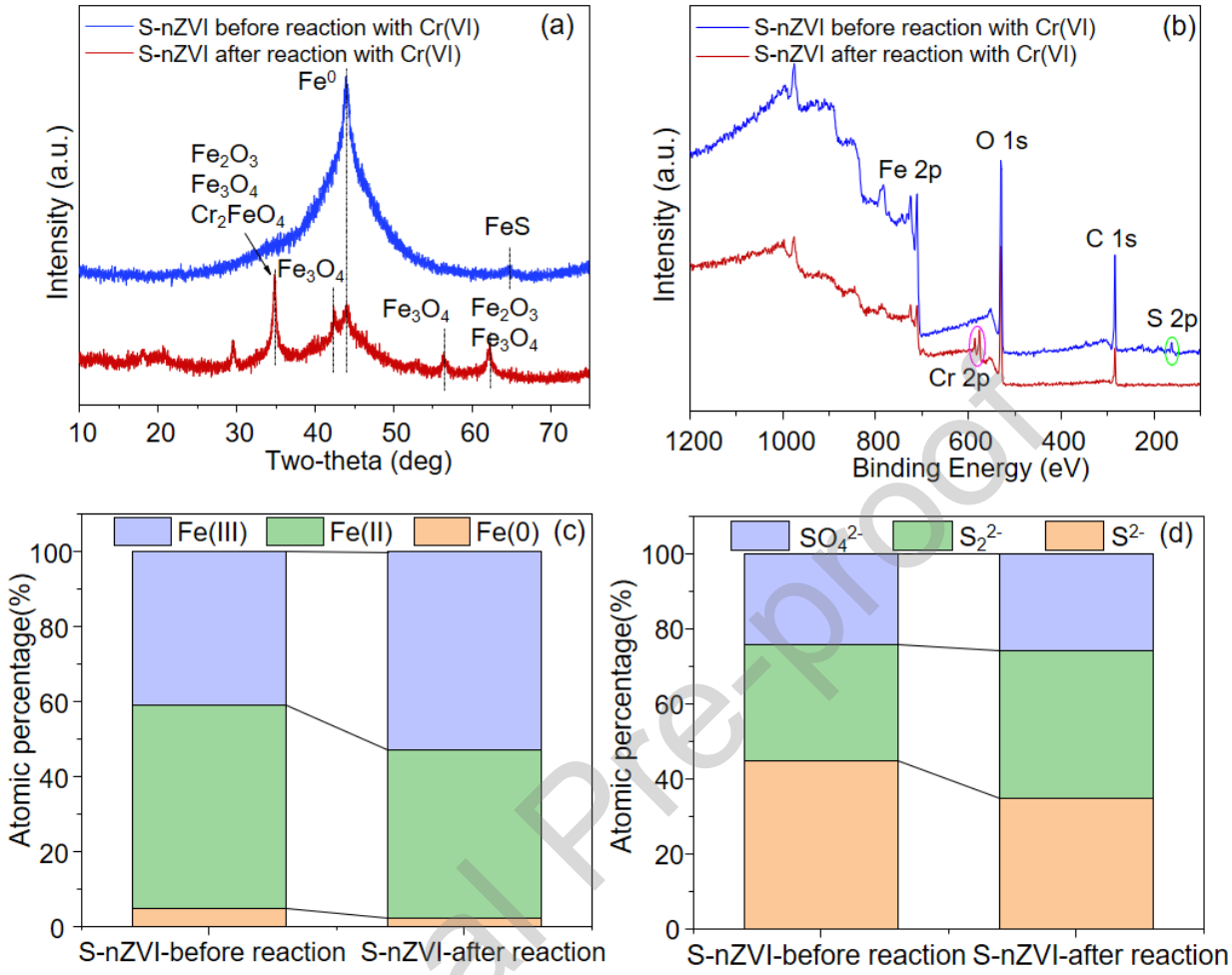

Fig. 2. (a) XRD patterns and (b) XPS patterns of S-nZVI before and after reaction with Cr(VI). (c) Fe species changes and (d) S species changes on the surface of S-nZVI. (S-nZVI=0.25 g/L, Cr(VI) concentration=100 mg/L, solution volume = 20 mL, pH = 5.8, equilibrium time = 144 h).

The Cr 2p XPS in Fig. S8b indicated the presence of only Cr(III) on the surface of the S-nZVI, supporting the notion that Cr(VI) was reduced by S-nZVI rather than undergoing simple adsorption. Moreover, the peak at around 710 eV and 724 eV aligned with Fe $2p_{3/2}$ and Fe $2p_{1/2}$, respectively (Fig. S8c). The peak at 719 eV represented a shake-up satellite (Sun et al., 2006). The appearance of feature peaks of Fe(II) and Fe(III) suggested that the materials were inevitably oxidized during the reaction with Cr(VI). On the other hand, iron oxides were not observed on the surface of S-

nZVI before the reaction with Cr(VI) in the XRD patterns (Fig. 2a), indicating either minimal oxidation of S-nZVI before the reaction with Cr(VI) or low crystallinity of iron oxides (Zhang et al., 2018b). The percentage of Fe(II) and Fe(0) on the surface of S-nZVI before the reaction with Cr(VI) were 54% and 5%, respectively, decreasing to 45% and 2% after reaction with Cr(VI) (Fig. 2c). At the same time, the percentage of Fe(III) increased from 41% to 53% after the treatment, supporting the oxidation of Fe(II) and Fe(0) to form Fe(III), participating in the reduction reaction of Cr(VI) (Eqs. 1-4) (Lv et al., 2019a; Manning et al., 2007). Similarly, S 2p XPS (Fig. S8d) was detected and the percentage of S^{2-} decreased from 45% to 35% after reaction with Cr(VI), while the percentage of S_2^{2-} and SO_4^{2-} increased from 31% to 39% and 24% to 26%, respectively (Fig. 2d). Therefore, it is also verified that S^{2-} greatly contributed to the reduction reaction of Cr(VI) (Eqs. 5-6). These results are generally consistent with the previously reported mechanisms suggesting that FeS is capable of reducing Cr(VI) (Gong et al., 2017; Lyu et al., 2017).

$$3Fe^0 + Cr_2O_7^{2-} + 7H_2O \rightarrow 3Fe^{2+} + 2Cr(OH)_3 + 8OH^- \quad (1)$$

$$6Fe^{2+} + Cr_2O_7^{2-} + 14H^+ \rightarrow 6Fe^{3+} + 2Cr^{3+} + 7H_2O \quad (2)$$

$$xCr^{3+} + (1\text{-}x)Fe^{3+} + 3H_2O \rightarrow (Cr_xFe_{1-x})(OH)_3(s) + 3H^+ \quad (3)$$

$$xCr^{3+} + (1\text{-}x)Fe^{3+} + 2H_2O \rightarrow Cr_xFe_{1-x}OOH(s) + 3H^+ \quad (4)$$

$$3S^{2-} + 8HCrO_4^- + 32H^+ \rightarrow 3SO_4^{2-} + 8Cr^{3+} + 20H_2O \quad (5)$$

$$HS^- + 2HCrO_4^- + 7H^+ = SO_3^{2-} + 2Cr^{3+} + 5H_2O \quad (6)$$

3.1.4 Responses of hydrochemical conditions to Cr(VI) remediation

As mentioned above, a portion of the surface of S-nZVI material had been oxidized forming Fe_2O_3 and Fe_3O_4. XPS analysis confirmed the successful reduction of Cr(VI) to Cr(III) with

immobilization of Cr(III) on the surface of S-nZVI. In order to gain further insights into the hydrochemical process of Cr(VI) removal by S-nZVI, changes in ORP and pH were monitored during the Cr(VI) treatment. As shown in Fig. 3a, the ORP changes differed from those in the control group. It rapidly decreased in the initial stage of the removal process, with the decreasing rate gradually slowing down, consistent with the concentration changes of Cr(VI). Without Cr(VI), the ORP remained at a negative value, slowly increasing to approximately 100 mV by the end in the control group. In contrast, the pH exhibited a swift initial rise; thereafter, it increased gradually as S-nZVI reacted with Cr(VI), as shown in Fig. 3b. In the control group without Cr(VI), the pH remained within the range of 6-7. The pH increase observed during the reaction between Cr(VI) and S-nZVI resulted from the substantial consumption of hydrogen ions (Eqs. 7-9) (Lyu et al., 2017; Montesinos et al., 2014). The Eh versus pH Pourbaix diagram of chromium species in the presence of iron and sulfur elements was generated using HSC Chemistry 6.0 software. The temperature and pressure were set as 25°C and 1 atm, respectively. The concentration of Fe, Cr and S elements was set as 1.0 mmol/L. It is indicated from Fig. 3c that Cr_2FeO_4 could be formed during the reduction and immobilization process of Cr(VI) by S-nZVI, which aligns with the XRD results.

$$2HCrO_4^- + 14H^+ + 3Fe^0(s) \rightarrow 2Cr^{3+} + 8H_2O + 3Fe^{2+} \quad (7)$$

$$FeS + H^+ \rightarrow Fe^{2+} + HS^- \quad (8)$$

$$HCrO_4^- + 7H^+ + 3Fe^{2+} \rightarrow Cr^{3+} + 3Fe^{3+} + 4H_2O \quad (9)$$

The rapid increase of solution pH from 5 to 11 suggests that little aqueous Fe(II) could be measured due to the formation of insoluble hydroxides at high pH (Shao et al., 2018). This observation is consistent with the overall decline in the concentration of Fe(II) seen in this study (Fig. 3d). When

S-nZVI encountered water, a portion of zero-valent iron would rapidly react with the H_2O to form Fe^{2+} (Xu et al., 2020), explaining the initially higher concentration of Fe(II) in Fig. 3d. Subsequently, Cr(VI) was rapidly reduced to Cr(III) by Fe(II), leading to a rapid decrease in the Fe(II) content, consistent with the initial stage's rapid reduction of Cr(VI). In the control group without Cr(VI), only a small amount of Fe(II) was consumed by dissolved oxygen, unlike the reaction with Cr(VI). As Cr(VI) continued to be reduced by Fe(II), the Fe(II) generated by the Fe(0) core was oxidized to Fe(III). A slight increase in the Fe(II) content was observed around the 8-hour mark may be due to the reduction of a fraction of Fe(III) to Fe(II) by bivalent sulfur ions on the surface of S-nZVI (Shao et al., 2018), along with the continuous supply of Fe(II) from the Fe(0) core of S-nZVI. Concurrently, the presence of FeS could obstruct the active sites on the Fe^0 surface, thereby slowing down the dissolution of the iron core and the formation of $(Cr_xFe_{1-x})(OH)_3$. Additionally, the precipitation of Cr(III)-Fe-S also consumed Fe(II), leading to a decrease in Fe(II) in the solution (Kim et al., 2011).

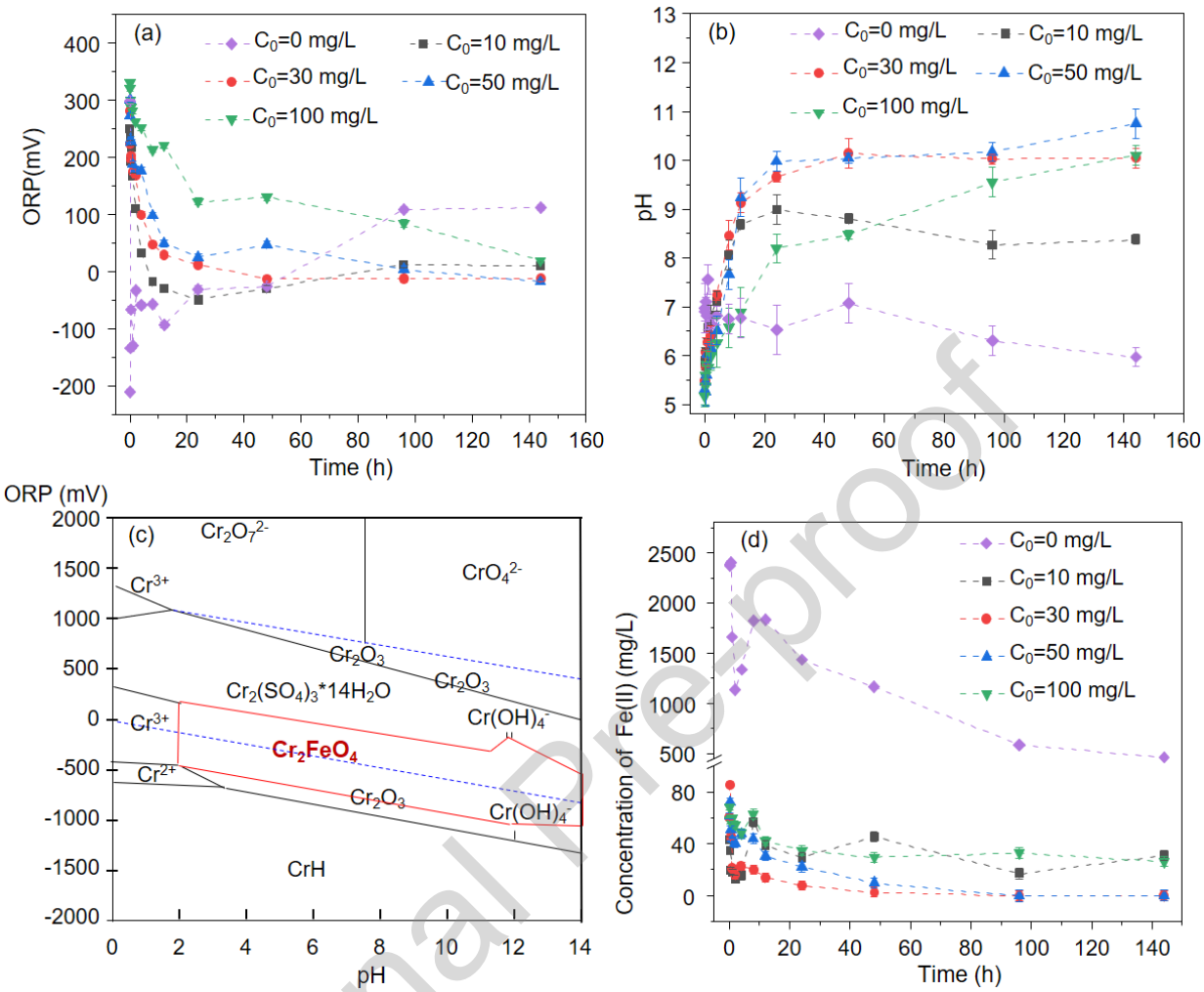

Fig. 3. (a) ORP changes and (b) pH changes during the removal of Cr(VI) by S-nZVI. (c) Eh-pH diagram of Cr-Fe-S system. (d) Dissolved Fe(II) changes during the removal of Cr(VI) by S-nZVI. (S-nZVI = 0.25 g/L, solution volume = 20 mL, and equilibrium time = 144 h).

A notably negative correlation between pH and ORP was observed (Fig. S9a) due to the substantial consumption of electrons and hydrogen ions during the reduction and immobilization process of Cr(VI) by S-nZVI (Montesinos et al., 2014). While the pH increase could potentially inhibit the reduction of Cr(VI) by S-nZVI (Lv et al., 2011), the deposition of the Cr-Fe precipitate on the surface of the material under alkaline conditions may enhance the adsorption of Cr(VI) on the surface of

S-nZVI (Zhang et al., 2018a). This could further contribute to the increased removal rate of Cr(VI). Throughout the process of Cr(VI) removal in the solution, the electrons, divalent iron, and bivalent sulfur continuously produced by S-nZVI could gradually accumulate, leading to a decrease in the ORP of the solution (Li et al., 2018). After Cr(VI) was treated by S-nZVI, the hydrochemical condition transitioned from a weakly acidic oxidation situation to an alkaline reduction status (Fig. S9b). It is essential to note that such interactions were only observed in the synthetic solutions, and variations may arise in real implementations with the presence of different background ions. These changes might also affect other processes, such as inhibiting the microbial activities in groundwater (Li et al., 2016; Zhang et al., 2020), and triggering other environmental issues, which needed to be further studied.

3.2. Breakthrough characterization

3.2.1 Efficiency of Cr(VI) remediation

The composite materials of S-nZVI and quartz sand were characterized using SEM (Fig. S10). S-nZVI particles were observed to be distributed on the surface of the quartz sand. The column breakthrough curves, which represent the normalized effluent Cr(VI) concentration (C/C_0) plotted as a function of pore volume (PV), are presented in Fig. 4a. When the mass of the mixed materials of S-nZVI and quartz sand ($m_{S\text{-}nZVI}$:m_{sand}=1:200) was 0, 2, 4, 6, and 8 g, respectively, the first detection times of Cr(VI) in the effluent were 0.8, 2.0, 3.7, 4.8, and 6.0 PVs after injecting the Cr(VI) solution. Subsequently, the concentration of Cr(VI) increased gradually, with the rate of increase being negatively correlated with the filling amount of the mixed S-nZVI materials. Once the injection of Cr(VI) was halted, the concentration of Cr(VI) in the outflow rapidly decreased to nearly zero, owing to the dilution and replenishment of the background solution. It is evident that the Cr(VI) content in the outflow decreases as the filling amount of the S-nZVI mixture increases,

and correspondingly, the dynamic removal of Cr(VI) by S-nZVI increases (Fig. 4b). Relevant parameters and results of the column experiments are listed in Table S3. It was observed that the cumulative removal of Cr(VI) increased from 0.73 mg to 2.28 mg (with a total Cr(VI) injection of 2.4 mg) as the S-nZVI mixed filler increased from 2 g to 8 g. Under the experimental conditions, the dynamic removal efficiency of Cr(VI) by S-nZVI exceeded 95% when the mixed filling materials were 8 g. This demonstrates that S-nZVI exhibits strong potential for the dynamic removal of Cr(VI) in a water environment. In addition, it is important to note that if the injection of Cr(VI) solution is prolonged until the C/C_0 ratio reaches approximately 1.0 and stabilizes, the concentration of Cr(VI) in effluent will continue to increase, similar to what was demonstrated in a previous study (Digiacomo et al., 2020). This is due to the diminishing removal efficiency resulting from the continuous consumption of S-nZVI.

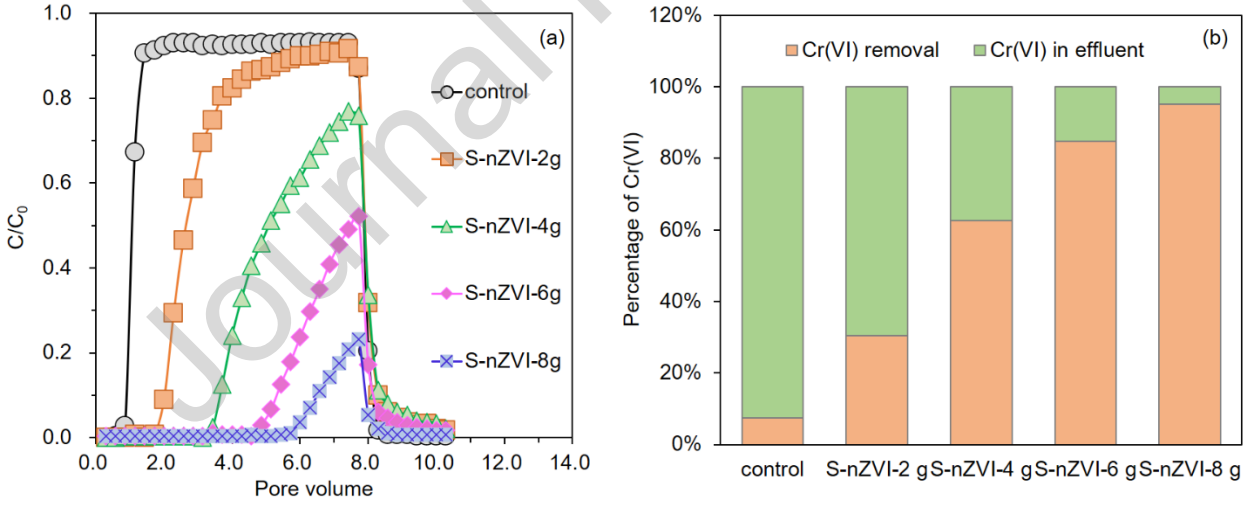

Fig. 4. The dynamic removal of Cr(VI) by S-nZVI in the sand column. (a) The concentration changes of Cr(VI) with the pore volume of Cr(VI) injection. (b) The total removal capacity of Cr(VI).

3.2.2 Utilization ratio and characterization of S-nZVI

The utilization ratio of S-nZVI material is defined as the percentage of actual removal capacity of Cr(VI) by S-nZVI per unit mass compared to its maximum removal capacity of 112.4 mg/g, as determined in the batch experiment. Based on this result, the utilization ratio of S-nZVI materials in the column experiment was calculated. The results in Fig. S11 show that the utilization ratios of S-nZVI materials in the column experiment were 65.0%, 67.0%, 60.5%, and 50.9% when the mixed filling materials were 0, 2, 4, 6, and 8 g, respectively. This indicates that increasing the amount of mixed filling materials did not lead to an increase in the utilization ratio of S-nZVI material. Hence, to enhance the utilization ratio of S-nZVI materials for Cr(VI) remediation, various factors, including the initial concentration of Cr(VI) and hydrochemical conditions, need to be taken into account. Furthermore, certain S-nZVI materials may not directly interact with the Cr(VI) solution, depending on their placement within the columns, such as being near dead-ends or in regions with stagnant flow, which might explain why the utilization ratios of S-nZVI materials did not reach 100% during the Cr(VI) remediation process (Digiacomo et al., 2020).

After the column tests, the filled packing materials were collected and subjected to SEM-EDX mapping, with the results presented in Fig. 5. Following Cr(VI) treatment, a significant presence of Fe and O elements was observed. This observation aligns with the expected formation of iron oxides or hydroxides as a result of Cr(VI) removal by S-nZVI. Notably, there was a clear presence of Cr on the surface of the filled packing materials, suggesting that Cr(VI) either interacted with S-nZVI in the sand column or that the reduction product of Cr(VI) was deposited in the sand column through adsorption and complexation (Xu et al., 2021). However, a relatively low quantity of S was observed on the surface of the packed materials after reaction with Cr(VI). This may be attributed

to S being actively involved in the Cr(VI) removal process by S-nZVI, subsequently transforming into soluble forms such as SO_4^{2-} or SO_3^{2-}, making it easier for transport through the sand column (Gong et al., 2017; Lyu et al., 2017).

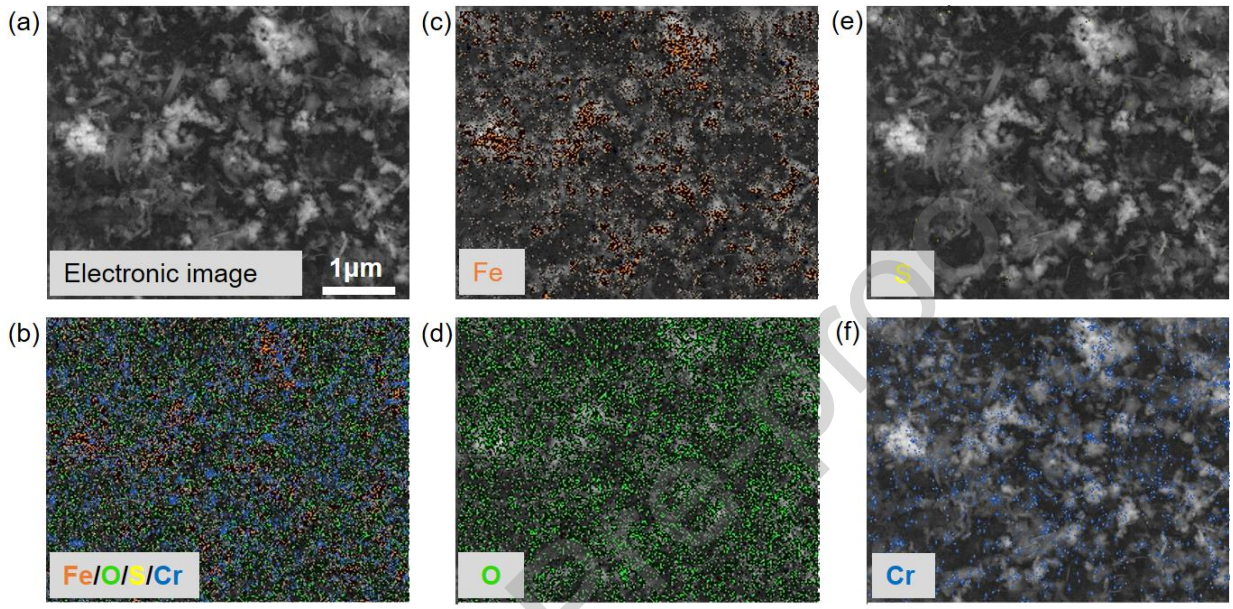

Fig. 5. Characteristic of S-nZVI filled packing materials after reaction with Cr(VI). (a) Electronic image. (b) Total elemental mappings of Fe, O, S and Cr. (c-f) Elemental mappings of Fe, O, S and Cr.

3.3. Molecular insight on Cr(VI) removal processes

3.3.1 Binding energy and Bader charges

To further elucidate the reaction mechanism between Cr(VI) and S-nZVI material, DFT calculations were conducted to determine the binding energy between different Cr species and S-nZVI (Fig. 6a). Given that $Cr_2O_7^{2-}$ is a prominent species in Cr(VI) solution prepared with $K_2Cr_2O_7$ and that, at an initial pH of 5.5±0.4, $HCrO_4^-$ is the predominant form of Cr(VI) (Dinda and Saha, 2015). Therefore, $Cr_2O_7^{2-}$ and $HCrO_4^-$ were chosen as the representative reactants for Cr(VI), while $Cr(OH)_3$ was selected to represent Cr(III) as a reaction product. Based on the characteristics of S-

nZVI before reaction with Cr(VI), a minor peak of FeS was evident in Fig. 2a, and S^{2-} was the predominant S species observed in Fig. 2d. In addition, when Na_2S alone was employed as the sulfidation species in the two-step synthesis method for producing S-nZVI material, FeS was the primary iron sulfide on the surface of S-nZVI (Fan et al., 2013). Therefore, it is reasonable to assume that FeS is the primary component of the surface of S-nZVI, which was chosen for the binding energy calculations. In a previous study, the binding energy of CrO_4^{2-} on the FeS surface was reported as -3.23 eV, indicating a strong reactivity in chemical adsorption (Ji et al., 2024). In this study, the binding energy of $HCrO_4^-$ on the FeS surface was calculated to be -2.29 eV, which aligns with the value reported in a previous study of -1.82 eV (Liu et al., 2022). The theoretical results revealed a preference for the combination of FeS with $Cr_2O_7^{2-}$ over $HCrO_4^-$, as evidenced by the lower binding energy between FeS and $Cr_2O_7^{2-}$ (-5.11 eV) compared to FeS and $HCrO_4^-$ (-2.29 eV). Considering that $Cr_2O_7^{2-}$ is the initial species in the Cr(VI) solution, this finding may explain the initial fast reaction rate observed in the batch experiment when Cr(VI) was removed by S-nZVI. The binding energy between FeS and $Cr(OH)_3$ was calculated to be -2.746 eV, indicating the binding of $Cr(OH)_3$ with S-nZVI is an exothermic reaction, lowering the overall energy to a more stable state. Therefore, $Cr(OH)_3$ is inclined to be deposited on the surface of S-nZVI material, achieving the immobilization of Cr(VI). Bader charges of $Cr_2O_7^{2-}$, $HCrO_4^-$ and $Cr(OH)_3$ were calculated to further explore the charge transfer during the Cr(VI) removal process by S-nZVI (Fig. 6b). The initial $Cr_2O_7^{2-}$ obtained 1.485 electronics from FeS coating on the surface of S-nZVI, indicating a redox reaction in the presence of H^+. In contrast, almost no charge transfer occurred for $Cr(OH)_3$, signifying its immobilization on the surface of the S-nZVI material and maintenance in a relatively stable chemical state. As for another important Cr(VI) species $HCrO_4^-$, it gained 0.948 electronics from FeS, resulting in its reduction.

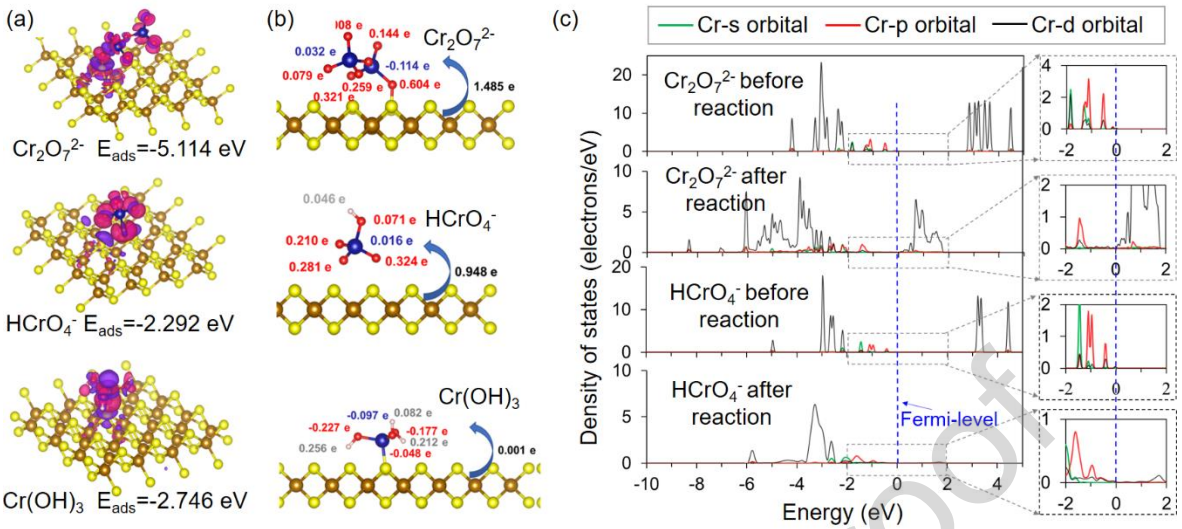

Fig. 6. DFT calculations of (a) the binding energy between Cr species and S-nZVI, (b) the Bader charges of $Cr_2O_7^{2-}$, $HCrO_4^-$ and $Cr(OH)_3$, and (c) partial density of states of Cr(VI) species before and after reaction on the surface of S-nZVI.

3.3.2 PDOS analysis and Cr(VI) reduction pathway

To gain further insights into the nature of the interaction between Cr species and S-nZVI during the reaction, projected density of states (PDOS) analysis was carried out for selected Cr (VI) species on FeS. The chosen Cr(VI) species, namely $Cr_2O_7^{2-}$, and $HCrO_4^-$, are the main initial components in the reaction system, exhibiting different binding energies when adsorbed on the surface of S-nZVI. Fig. 6c illustrates the PDOS for the Cr atom of Cr (VI) before and after reaction with S-nZVI. Analysis of the PDOS curves reveals the involvement of s, p and d orbitals of Cr during the reaction with S-nZVI. As for $Cr_2O_7^{2-}$, the PDOS of Cr collectively shifts towards lower energy after reaction with S-nZVI, which confirms the participation of all three orbitals of Cr in the interaction between $Cr_2O_7^{2-}$ and S-nZVI. In addition, an increase in the number of p orbital peaks within the energy range of -6 eV~-1 eV suggests enhanced electron localization for $Cr_2O_7^{2-}$ after reaction, indicating a change in the electron density of Cr atom in $Cr_2O_7^{2-}$ upon reaction with

S-nZVI. Furthermore, it is observed that p orbital peaks for $Cr_2O_7^{2-}$ transition from narrow and sharp peaks to broader peaks after reaction, suggesting a higher electron density of the Cr atom in $Cr_2O_7^{2-}$ before the reaction, promoting electron transfer during the reaction (Zhang et al., 2023). The peaks of the d orbital also shift towards the Fermi-level after the reaction. As for $HCrO_4^-$, the PDOS of Cr slightly shifts towards lower energy levels after the reaction with S-nZVI, potentially due to the relatively weaker binding energy compared with $Cr_2O_7^{2-}$. Notably, peaks above the Fermi-level disappear, confirming the involvement of the Cr d orbital in the interaction between $HCrO_4^-$ and S-nZVI.

As discussed above, the characterization analysis of S-nZVI materials after reaction with Cr(VI) indicated the reduction of Cr(VI) to Cr(III) facilitated by divalent iron and sulfur, or through direct electron transfer from Fe(0) core. The changes in hydrochemical conditions also demonstrated that the process of Cr(VI) removal by S-nZVI consumed a considerable amount of H^+. To explore the potential reduction pathway of Cr(VI) by S-nZVI, DFT calculations were employed (Fig. 7). According to a previous study, $Cr_2O_7^{2-}$ possesses some axial symmetry O atoms, identified as the most favourable sites for the proton addition (Gao et al., 2022). In this proposed pathway, an axial symmetry O in the $Cr_2O_7^{2-}$ initially bonds with a proton and gains an electron. Subsequently, another proton would bond with the same O, concurrently releasing an H_2O molecule and generating $Cr_2O_6^{2-}$. The generated $Cr_2O_6^{2-}$ would then undergo cleavage into two CrO_3^- with a 1.47 eV decrease in energy. The unstable CrO_3^- would be further reduced step by step in the presence of electrons and H^+ until $Cr(OH)_3$ is formed. Calculations based on Eq. 2 reveal that 6 mol e^- and 14 mol H^+ would be consumed during the removal of $Cr_2O_7^{2-}$, resulting in the reduction to Cr^{3+} and the production of H_2O. As for another Cr(VI) species, $HCrO_4^-$, a proton would bond with it

and release an H_2O molecule. Simultaneously, CrO_3^- is generated with a 0.36 eV decrease in energy. The subsequent reduction pathway mirrors that of $Cr_2O_7^{2-}$. Calculations based on Eq. 9 indicate that 3 mol e^- and 7 mol H^+ would be consumed during the removal of $HCrO_4^-$, leading to the reduction to Cr^{3+} and the production of H_2O.

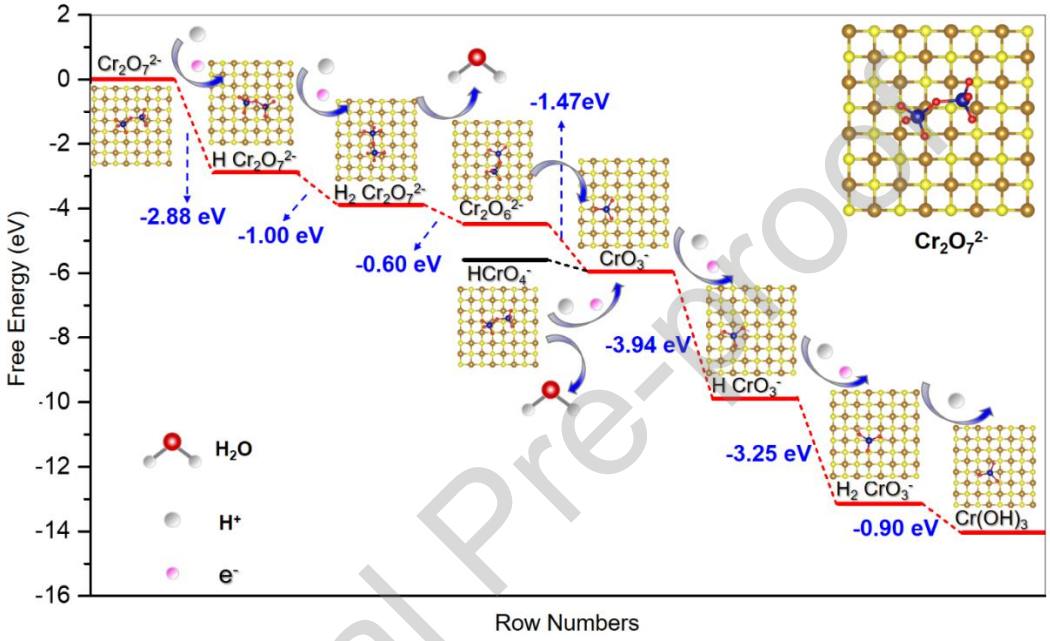

Fig. 7. Cr(VI) reduction pathway and energy level structure.

3.4. Summarised process mechanisms and implementation potentials

In conclusion, the mechanism underlying the removal of Cr(VI) by S-nZVI differs from that observed with nZVI, attributed to the presence of an active layer of iron sulfides instead of a passive iron oxides film on the surface of S-nZVI. This layer of iron sulfides serves as a source of Fe(II) and S^{2-} species, both acting as agents for reduction and precipitation (Wu et al., 2017). In a recent study on the interaction between FeS and Cr, the authors found that Fe(II) was the predominant reducing agent, while S species in FeS also served as electron donors for Cr(VI) (Ji et al., 2024). Although both Fe and S in FeS contribute to the reduction of Cr(VI), some researches emphasized the role of Fe in FeS (Liu et al., 2022; Wang et al., 2023), while others suggested that Cr(VI) was

primarily reduced by S in FeS (Ji et al., 2024). Therefore, it is challenging to conclusively determine which species in S-nZVI, Fe or S, plays the dominant role. In this study, Cr(VI) removal by S-nZVI was demonstrated in both batch and column experiments, where both Fe(II) and S^{2-} played crucial roles in the reduction and immobilization of Cr(VI). The reaction process altered hydro-chemical conditions, subsequently influencing the removal efficiency of Cr(VI) by S-nZVI. A proposed process mechanism for Cr(VI) removed by S-nZVI is depicted in Fig. 8. The three main phases include Cr(VI) diffusion and adsorption onto the surface of the S-nZVI particles due to the nanometer-scale size and electrostatic interaction; direct electron transfer from Fe^0 core, Fe(II), and S^{2-} causing reduction of Cr(VI) to Cr(III) along with concurrent pH increase and ORP decrease; and finally, coprecipitation of Cr(III) and Fe(III) due to the pH exceeding 4.0 (Lv et al., 2019a). Notably, the processes of adsorption and reduction occur concurrently rather than independently. According to the previous studies (Liu et al., 2022; Wang et al., 2023), as the reaction proceeds, the S-nZVI material undergoes continuous oxidation, resulting in an increase in Cr(VI) adsorption while the reduction of Cr(VI) decreases. The simultaneous occurrence of adsorption, reduction, and coprecipitation results in the sequestration of aqueous Cr(VI). Although a similar reaction mechanism for the removal of Cr(VI) by S-nZVI was presented in some other literature (Lv et al., 2019a; Wu et al., 2017), and field-scale studies (Brumovský et al., 2021; Garcia et al., 2020) have showcased the superior performance of S-nZVI in Cr(VI) removal, this study focused on elucidating the molecular-level mechanism between S-nZVI and Cr(VI). It also highlights the changes in pH and ORP during the process of Cr(VI) removal by S-nZVI. While dilution and advection in large quantities of groundwater may alleviate the impact of pH and ORP changes, future implementation warrants additional investigation, modelling, and materials development to minimize environmental impact.

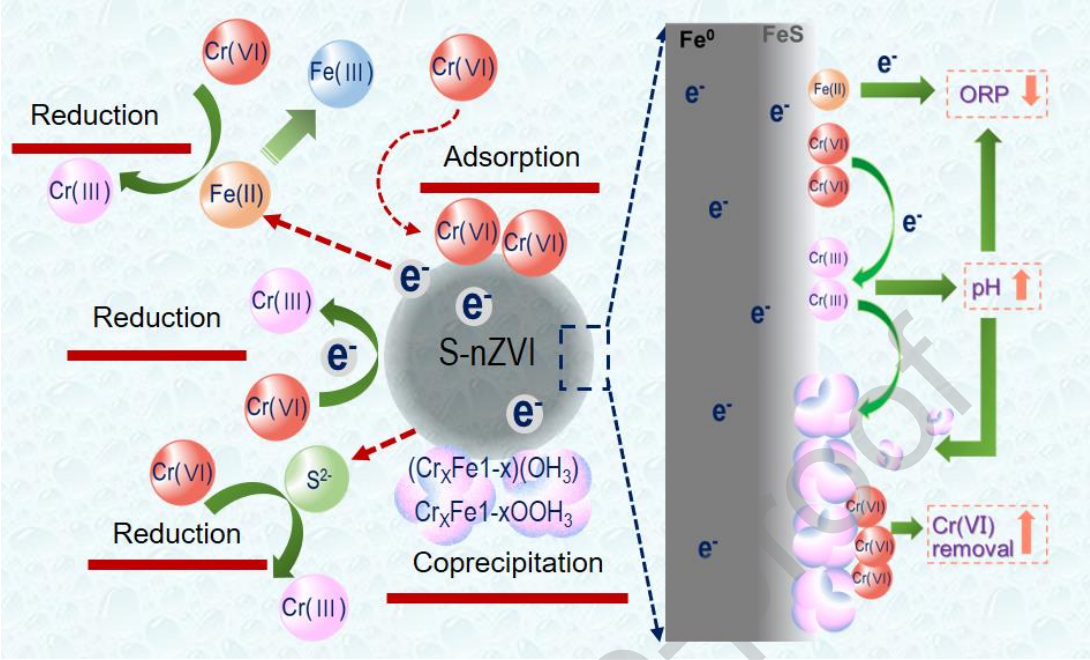

Fig. 8. Schematic diagram of the process mechanisms of Cr(VI) treated by S-nZVI.

4. Conclusions

S-nZVI material exhibits desirable efficacy of 112.4 mg/g in the removal of Cr(VI) when the initial Cr(VI) concentration is 100 mg/L. The presence of a sulfate layer on the surface of S-nZVI facilitates the efficient action of Fe(II) and S^{2-} species, leading to unique precipitation of Cr_2FeO_4/Cr(III) and enhancing the removal of Cr(VI). Substantial changes in ORP and pH levels during the Cr(VI) removal process by S-nZVI indicate a close relationship between hydrochemical reactive dynamics and the application of S-nZVI for addressing Cr(VI) pollution in water. The results of the column experiment highlight the strong in-situ Cr(VI) remediation capacity of S-nZVI in contaminated groundwater since the remediation efficiency could reach to 95% when the mixed filling materials of S-nZVI and quartz sand were 8 g. Furthermore, stoichiometric DFT calculations reveal molecular-level interactions between Cr(VI) and S-nZVI during the removal process, providing evidence for multi-step reduction pathways. Analysis of the process mechanism

demonstrates that the removal of Cr(VI) by S-nZVI involves adsorption, reduction, and coprecipitation with the concurrent pH increase and ORP decrease. The outstanding reduction and immobilization capabilities, combined with good selectivity of electron, underscore the significant potential of S-nZVI in remediating Cr(VI)-contaminated water.

Acknowledgement

This research was supported by National Natural Science Foundation of China (42277189, 42172284) and Science and Technology Development Fund, Macao S.A.R (FDCT) (0033/2022/A1).

Reference

Alam, M.S., Han, B., Pichtel, J., 2020. Assessment of soil and groundwater contamination at a former Tannery district in Dhaka, Bangladesh. Environmental Geochemistry and Health. 42(7), 1905-1920.

Alidokht, L., Khataee, A., Reyhanitabar, A., Oustan, S., 2011. Reductive removal of Cr(VI) by starch-stabilized Fe^0 nanoparticles in aqueous solution. Desalination. 270(1-3), 105-110.

Bhattacharjee, S., Ghoshal, S., 2018. Optimal design of sulfidated nanoscale zerovalent iron for enhanced trichloroethene degradation. Environmental science & technology. 52(19), 11078-11086.

Bhattacharya, A., Naiya, T., Mandal, S., Das, S., 2008. Adsorption, kinetics and equilibrium studies on removal of Cr(VI) from aqueous solutions using different low-cost adsorbents. Chemical engineering journal. 137(3), 529-541.

Brumovský, M., Oborná, J., Lacina, P., Hegeduš, M., Sracek, O., Kolařík, J., Petr, M., Kašlík, J., Hofmann, T., Filip, J., 2021. Sulfidated nano-scale zerovalent iron is able to effectively reduce in situ hexavalent chromium in a contaminated aquifer. Journal of Hazardous Materials. 405, 124665.

Cao, Z., Liu, X., Xu, J., Zhang, J., Yang, Y., Zhou, J., Xu, X., Lowry, G.V., 2017. Removal of antibiotic florfenicol by sulfide-modified nanoscale zero-valent iron. Environmental Science & Technology. 51(19), 11269-11277.

Digiacomo, F., Tobler, D.J., Held, T., Neumann, T., 2020. Immobilization of Cr(VI) by sulphate green rust and sulphidized nanoscale zerovalent iron in sand media: batch and column studies. Geochemical transactions. 21, 1-12.

Dinda, D., Saha, S.K., 2015. Sulfuric acid doped poly diaminopyridine/graphene composite to remove high concentration of toxic Cr(VI). Journal of hazardous materials. 291, 93-101.

Dong, D., Zhao, X., Hua, X., Liu, J., Gao, M., 2009. Investigation of the potential mobility of Pb, Cd and Cr(VI) from moderately contaminated farmland soil to groundwater in Northeast, China. Journal of Hazardous Materials. 162(2-3), 1261-1268.

Dong, H., Deng, J., Xie, Y., Zhang, C., Jiang, Z., Cheng, Y., Hou, K., Zeng, G., 2017. Stabilization of nanoscale zero-valent iron (nZVI) with modified biochar for Cr(VI) removal from aqueous solution. Journal of Hazardous Materials. 332, 79-86.

Fan, D., Anitori, R.P., Tebo, B.M., Tratnyek, P.G., Lezama Pacheco, J.S., Kukkadapu, R.K., Engelhard, M.H., Bowden, M.E., Kovarik, L., Arey, B.W., 2013. Reductive sequestration of pertechnetate ($^{99}TcO_4^-$) by nano zerovalent iron (nZVI) transformed by abiotic sulfide. Environmental Science & Technology. 47(10), 5302-5310.

Gao, G., Zhang, L., Shi, Y., Yang, S., Wang, G., Xu, H., Ding, D., Chen, R., Jin, P., Wang, X.C., 2022. Mutual-activation between Zero-Valent iron and graphitic carbon for Cr(VI) Removal: Mechanism and inhibition of inherent Side-reaction. Journal of Colloid and Interface Science. 608, 588-598.

Garcia, A.N., Boparai, H.K., de Boer, C.V., Chowdhury, A.I., Kocur, C.M., Austrins, L.M., Herrera, J., O'Carroll, D.M., 2020. Fate and transport of sulfidated nano zerovalent iron (S-nZVI): a field study. Water Research. 170, 115319.

Garcia, A.N., Zhang, Y., Ghoshal, S., He, F., O'Carroll, D.M., 2021. Recent advances in sulfidated zerovalent iron for contaminant transformation. Environmental Science & Technology. 55(13), 8464-8483.

Gong, Y., Gai, L., Tang, J., Fu, J., Wang, Q., Zeng, E.Y., 2017. Reduction of Cr(VI) in simulated groundwater by FeS-coated iron magnetic nanoparticles. Science of the Total Environment. 595, 743-751.

Goswami, S., Ghosh, U.C., 2005. Studies on adsorption behaviour of Cr(VI) onto synthetic hydrous stannic oxide. water SA. 31(4), 597-602.

Guan, X., Sun, Y., Qin, H., Li, J., Lo, I.M., He, D., Dong, H., 2015. The limitations of applying zero-valent iron technology in contaminants sequestration and the corresponding countermeasures: the development in zero-valent iron technology in the last two decades (1994–2014). Water research. 75, 224-248.

Han, Y., Yan, W., 2016. Reductive Dechlorination of Trichloroethene by Zero-valent Iron Nanoparticles: Reactivity Enhancement through Sulfidation Treatment. Environmental Science & Technology. 12992.

Hossain, M.A., Kumita, M., Michigami, Y., Mori, S., 2005. Kinetics of Cr(VI) adsorption on used black tea leaves. Journal of chemical engineering of Japan. 38(6), 402-408.

Huang, X., Niu, X., Zhang, D., Li, X., Li, H., Wang, Z., Lin, Z., Fu, M., 2022. Fate and mechanistic insights into nanoscale zerovalent iron (nZVI) activation of sludge derived biochar reacted with Cr(VI). Journal of Environmental Management. 319, 115771.

Hüffer, T., Kah, M., Hofmann, T., Schmidt, T.C., 2013. How redox conditions and irradiation affect sorption of PAHs by dispersed fullerenes (nC60). Environmental science & technology. 47(13), 6935-6942.

Ji, H., Gao, S., Chen, L., Zhao, X., Zhao, D., 2024. New insights of FeS–Cr interaction in sequestration remediation: Model, mechanism, and DFT calculation. Journal of Cleaner Production. 435, 140484.

Jin, H., Meng, D., Liu, X., Liang, Y., Yin, H., Liu, H., 2018. Response of soil fungal community to long-term chromium contamination. Transactions of Nonferrous Metals Society of China. 28(9), 1838-1846.

Kim, E., Kim, J., Azad, A., Chang, Y., 2011. Facile synthesis and characterization of Fe/FeS nanoparticles for environmental applications. ACS applied materials & interfaces. 3(5), 1457-1462.

Li, J., Zhang, X., Liu, M., Pan, B., Zhang, W., Shi, Z., Guan, X., 2018. Enhanced Reactivity and Electron Selectivity of Sulfidated Zerovalent Iron toward Chromate under Aerobic Conditions. Environmental Science & Technology. 52(5), 2988-2997.

Li, T., Zhu, F., Gao, Y., Iribagiza, M.R., Hu, G., Guan, J., 2024. Efficient elimination of Cr(VI) in groundwater using nano zero-valent iron synthesized with Ginkgo biloba extracts: enhanced mechanism and reduced toxicity. Environmental Science: Water Research & Technology. 10(2), 339-352.

Li, T., Zhu, F., Liang, W., Hu, G., Deng, X., Xue, Y., Guan, J., 2022. Simultaneous removal of p-nitrophenol and Cr(VI) using biochar supported green synthetic nano zero valent iron-copper: mechanistic insights and toxicity evaluation. Process Safety and Environmental Protection. 167, 629-640.

Li, Y., Zhang, Z., Fei, Y., Chen, H., Qian, Y., Dun, Y., 2016. Investigation of quality and pollution characteristics of groundwater in the Hutuo River Alluvial Plain, North China Plain. Environmental Earth Sciences. 75(7), 581.

Liu, Y., Gan, H., Tian, L., Liu, Z., Ji, Y., Zhang, T., Alvarez, P.J., Chen, W., 2022. Partial oxidation of FeS nanoparticles enhances Cr(VI) sequestration. Environmental Science & Technology. 56(19), 13954-13963.

Liu, Y., Lowry, G.V., 2006. Effect of particle age (Fe^0 content) and solution pH on NZVI reactivity: H_2 evolution and TCE dechlorination. Environmental science & technology. 40(19), 6085-6090.

Luo, J., Meng, X., Crittenden, J., Qu, J., Hu, C., Liu, H., Peng, P., 2018. Arsenic adsorption on α-MnO_2 nanofibers and the significance of (100) facet as compared with (110). Chemical Engineering Journal. 331, 492-500.

Luo, S., Lu, T., Peng, L., Shao, J., Zeng, Q., Gu, J.-D., 2014. Synthesis of nanoscale zero-valent iron immobilized in alginate microcapsules for removal of Pb(II) from aqueous solution. Journal of Materials Chemistry A. 2(37), 15463-15472.

Lv, D., Zhou, J., Cao, Z., Xu, J., Liu, Y., Li, Y., Yang, K., Lou, Z., Lou, L., Xu, X., 2019a. Mechanism and influence factors of chromium (VI) removal by sulfide-modified nanoscale zerovalent iron. Chemosphere. 224, 306-315.

Lv, D., Zhou, X., Zhou, J., Liu, Y., Li, Y., Yang, K., Lou, Z., Baig, S.A., Wu, D., Xu, X., 2018. Design and characterization of sulfide-modified nanoscale zerovalent iron for cadmium (II) removal from aqueous solutions. Applied Surface Science. 442, 114-123.

Lv, X., Jiang, X., Jiang, G., Xu, X., 2011. Removal of chromium(VI) from wastewater by nanoscale zero-valent iron particles supported on multiwalled carbon nanotubes. Chemosphere. 85(7), 1204-1209.

Lv, Z., Fan, Q., Xie, Y., Chen, Z., Alsaedi, A., Hayat, T., Wang, X., Chen, C., 2019b. MOFs-derived magnetic chestnut shell-like hollow sphere NiO/Ni@ C composites and their removal performance for arsenic (V). Chemical Engineering Journal. 362, 413-421.

Lyu, H., Tang, J., Huang, Y., Gai, L., Zeng, E.Y., Liber, K., Gong, Y., 2017. Removal of hexavalent chromium from aqueous solutions by a novel biochar supported nanoscale iron sulfide composite. Chemical Engineering Journal. 322, 516-524.

Manning, B.A., Kiser, J.R., Kwon, H., Kanel, S.R., 2007. Spectroscopic investigation of Cr(III)- and Cr(VI)-treated nanoscale zerovalent iron. Environmental science & technology. 41(2), 586-592.

Mohanty, K., Jha, M., Meikap, B., Biswas, M., 2005. Removal of chromium (VI) from dilute aqueous solutions by activated carbon developed from Terminalia arjuna nuts activated with zinc chloride. Chemical Engineering Science. 60(11), 3049-3059.

Montesinos, V.N., Quici, N., Halac, E.B., Leyva, A.G., Custo, G., Bengio, S., Zampieri, G., Litter, M.I., 2014. Highly efficient removal of Cr(VI) from water with nanoparticulated zerovalent iron: understanding the Fe(III)–Cr(III) passive outer layer structure. Chemical Engineering Journal. 244, 569-575.

N. Xafenias, Y. Zhang, Banks, C.J., 2015. Evaluating hexavalent chromium reduction and electricity production in microbial fuel cells with alkaline cathodes. International Journal of Environmental ence and Technology. 12(8), 2435-2446.

Nazir, R., Khan, M., Masab, M., Rehman, H.U., Rauf, N.U., Shahab, S., Ameer, N., Sajed, M., Ullah, M., Rafeeq, M., 2015. Accumulation of heavy metals (Ni, Cu, Cd, Cr, Pb, Zn, Fe) in the soil, water and plants and analysis of physico-chemical parameters of soil and water collected from Tanda Dam Kohat. Journal of pharmaceutical sciences and research. 7(3), 89.

Pandey, P., Sharma, S., Sambi, S., 2010. Kinetics and equilibrium study of chromium adsorption on zeoliteNaX. International Journal of Environmental Science & Technology. 7, 395-404.

Pérez-Candela, M., Martín-Martínez, J., Torregrosa-Maciá, R., 1995. Chromium (VI) removal with activated carbons. Water Research. 29(9), 2174-2180.

Periasamy, K., Srinivasan, K., Murugan, P., 1991. Studies on chromium (VI) removal by activated groundnut husk carbon. Indian J. Environ. Health. 33(4), 433-439.

Puls, R.W., Paul, C.J., Powell, R.M., 1999. The application of in situ permeable reactive (zero-valent iron) barrier technology for the remediation of chromate-contaminated groundwater: a field test. Applied Geochemistry. 14(8), 989-1000.

Rajajayavel, S.R.C., Ghoshal, S., 2015. Enhanced reductive dechlorination of trichloroethylene by sulfidated nanoscale zerovalent iron. Water research. 78, 144-153.

Shao, Q., Xu, C., Wang, Y., Huang, S., Zhang, B., Huang, L., Fan, D., Tratnyek, P.G., 2018. Dynamic interactions between sulfidated zerovalent iron and dissolved oxygen: Mechanistic insights for enhanced chromate removal. Water research. 135, 322-330.

Shen, H., Chen, J., Dai, H., Wang, L., Hu, M., Xia, Q., 2013. New insights into the sorption and detoxification of chromium (VI) by tetraethylenepentamine functionalized nanosized magnetic polymer adsorbents: mechanism and pH effect. Industrial & Engineering Chemistry Research. 52(36), 12723-12732.

Sherene, T., 2010. Mobility and transport of heavy metals in polluted soil environment. Biological forum—an international journal. 2(2), 112-121.

Song, X., Zhang, Y., Cao, N., Sun, D., Zhang, Z., Wang, Y., Wen, Y., Yang, Y., Lyu, T., 2021. Sustainable Chromium (VI) Removal from Contaminated Groundwater Using Nano-Magnetite-Modified Biochar via Rapid Microwave Synthesis. Molecules. 26(1), 103.

Su, J., Bi, L., Wang, C., Lyu, T., Pan, G., 2019. Enhancement of cadmium removal by oxygen-doped carbon nitride with molybdenum and sulphur hybridization. Journal of colloid and interface science. 556, 606-615.

Su, J., Lyu, T., Yi, H., Bi, L., Pan, G., 2020. Superior arsenate adsorption and comprehensive investigation of adsorption mechanism on novel Mn-doped $La_2O_2CO_3$ composites. Chemical Engineering Journal. 391, 123623.

Sun, P., Wang, Z., An, S., Zhao, J., Yan, Y., Zhang, D., Wu, Z., Shen, B., Lyu, H., 2022. Biochar-supported nZVI for the removal of Cr(VI) from soil and water: advances in experimental research and engineering applications. Journal of Environmental Management. 316, 115211.

Sun, Y., Li, X., Cao, J., Zhang, W., Wang, H.P., 2006. Characterization of zero-valent iron nanoparticles. Advances in colloid and interface science. 120(1-3), 47-56.
Tian, H., Huang, C., Wang, P., Wei, J., Li, X., Zhang, R., Ling, D., Feng, C., Liu, H., Wang, M., 2023. Enhanced elimination of Cr(VI) from aqueous media by polyethyleneimine modified corn straw biochar supported sulfide nanoscale zero valent iron: Performance and mechanism. Bioresource Technology. 369, 128452.
Wang, C., Yin, H., Bi, L., Su, J., Pan, G., 2019. Highly efficient and irreversible removal of cadmium through the formation of a solid solution. Journal of Hazardous Materials. 384, 121461.
Wang, Q., Yang, L., Jia, F., Li, Y., Song, S., 2018. Removal of Cd(II) from water by using nano-scale molybdenum disulphide sheets as adsorbents. Journal of molecular liquids. 263, 526-533.
Wang, T., Zhao, D., Liu, J., Zhang, T., Wang, X., Liu, T., Wang, S., Liu, G., Liu, B., Liu, Y., 2023. Effects of abiotic mineral transformation of FeS on the dynamic immobilization of Cr(VI) in oxic aquatic environments. Science of The Total Environment. 164991.
Wise Sr, J.P., Payne, R., Wise, S.S., LaCerte, C., Wise, J., Gianios Jr, C., Thompson, W.D., Perkins, C., Zheng, T., Zhu, C., 2009. A global assessment of chromium pollution using sperm whales (Physeter macrocephalus) as an indicator species. Chemosphere. 75(11), 1461-1467.
Wu, J., Wang, X., Zeng, R., 2017. Reactivity enhancement of iron sulfide nanoparticles stabilized by sodium alginate: taking Cr(VI) removal as an example. Journal of hazardous materials. 333, 275-284.
Xu, H., Gao, M., Hu, X., Chen, Y., Li, Y., Xu, X., Zhang, R., Yang, X., Tang, C., Hu, X., 2021. A novel preparation of S-nZVI and its high efficient removal of Cr(VI) in aqueous solution. Journal of Hazardous Materials. 416, 125924.
Xu, J., Avellan, A., Li, H., Liu, X., Lowry, G.V., 2020. Sulfur loading and speciation control the hydrophobicity, electron transfer, reactivity, and selectivity of sulfidized nanoscale zerovalent iron. Advanced Materials. 32(17), 1906910.
Xu, J., Cao, Z., Wang, Y., Zhang, Y., Gao, X., Ahmed, M.B., Zhang, J., Yang, Y., Zhou, J.L., Lowry, G.V., 2019a. Distributing sulfidized nanoscale zerovalent iron onto phosphorus-functionalized biochar for enhanced removal of antibiotic florfenicol. Chemical Engineering Journal. 359, 713-722.
Xu, J., Wang, Y., Weng, C., Bai, W., Jiao, Y., Kaegi, R.l., Lowry, G.V., 2019b. Reactivity, selectivity, and long-term performance of sulfidized nanoscale zerovalent iron with different properties. Environmental science & technology. 53(10), 5936-5945.
Yang, D., Deng, R., Chen, M., Liu, T., Luo, L., He, Q., Chen, Y., 2023. Biochar-based microporous nanosheets-mediated nanoconfinement for high-efficiency reduction of Cr(VI). Journal of Hazardous Materials. 459, 132283.
Yirsaw, B.D., Megharaj, M., Chen, Z., Naidu, R., 2016. Environmental application and ecological significance of nano-zero valent iron. Journal of Environmental Sciences. 44, 88-98.
Zhang, A., Shen, X., Yin, X., Li, X., Liu, Y., 2018a. Application of calcium peroxide for efficient removal of triamcinolone acetonide from aqueous solutions: mechanisms and products. Chemical Engineering Journal. 345, 594-603.
Zhang, H., Wang, X., Chen, C., Wang, Q., Yang, Y., Yong, S., 2010. Study on the polluting property of chrome residue contaminated sites in plateau section. Chinese Journal of Environmental Engineering. 4(4), 915-918.

Zhang, S., Hao, X., Tang, J., Hu, J., Deng, Y., Xu, M., Zhu, P., Tao, J., Liang, Y., Yin, H., 2020. Assessing chromium contamination in red soil: monitoring the migration of fractions and the change of related microorganisms. International journal of environmental research and public health. 17(8), 2835.

Zhang, S., Wu, M., Tang, T., Xing, Q., Peng, C., Li, F., Liu, H., Luo, X., Zou, J., Min, X., 2018b. Mechanism investigation of anoxic Cr(VI) removal by nano zero-valent iron based on XPS analysis in time scale. Chemical Engineering Journal. 335, 945-953.

Zhang, X., He, J., He, B., Sun, J., 2019a. Assessment, formation mechanism, and different source contributions of dissolved salt pollution in the shallow groundwater of Hutuo River alluvial-pluvial fan in the North China Plain. Environmental Science and Pollution Research. 26(35), 35742-35756.

Zhang, X., He, J., Huang, G., 2021. Distribution characteristics and cause analysis of iron and manganese in shallow groundwater in Shijiazhuang area. Earth Science Frontiers. 28(4), 206-218.

Zhang, Y., Duan, Z., Wang, X., Li, Y., Xu, C., 2023. Nitrogen modification enhances conductivity and reactivity of sulfidated zero-valent iron: Mechanism and Cr(VI) removal. Journal of Cleaner Production. 427, 139266.

Zhang, Y., Ma, H.-L., Peng, J., Zhai, M., Yu, Z.-Z., 2013. Cr(VI) removal from aqueous solution using chemically reduced and functionalized graphene oxide. Journal of Materials Science. 48(5), 1883-1889.

Zhang, Z., Gu, P., Zhang, M., Yan, S., Dong, L., Zhang, G., 2019b. Synthesis of a robust layered metal sulfide for rapid and effective removal of Sr^{2+} from aqueous solutions. Chemical Engineering Journal. 372, 1205-1215.

Zheng, X., Wu, Q., Huang, C., Wang, P., Cheng, H., Sun, C., Zhu, J., Xu, H., Ouyang, K., Guo, J., 2023. Synergistic effect and mechanism of Cd(II) and As(III) adsorption by biochar supported sulfide nanoscale zero-valent iron. Environmental Research. 231, 116080.

Zhou, L., Wang, K., Yi, Y., Fang, Z., 2023. Sophorolipid modification enables high reactivity and electron selectivity of nanoscale zerovalent iron toward hexavalent chromium. Journal of Environmental Management. 326, 116775.

Zhu, F., Lu, H., Li, T., He, S., Xu, H., 2024. Degradation on BDE209 in the soil by kaolin-supported sulfurized nano-zero-valent iron activated persulfate system: Insights mechanism and DFT calculations. Journal of Environmental Chemical Engineering. 12(1), 111882.

Declaration of Competing Interest

The authors declare that they have no known competing financial interests or personal relationships that could have appeared to influence the work reported in this paper.

Graphic Abstract

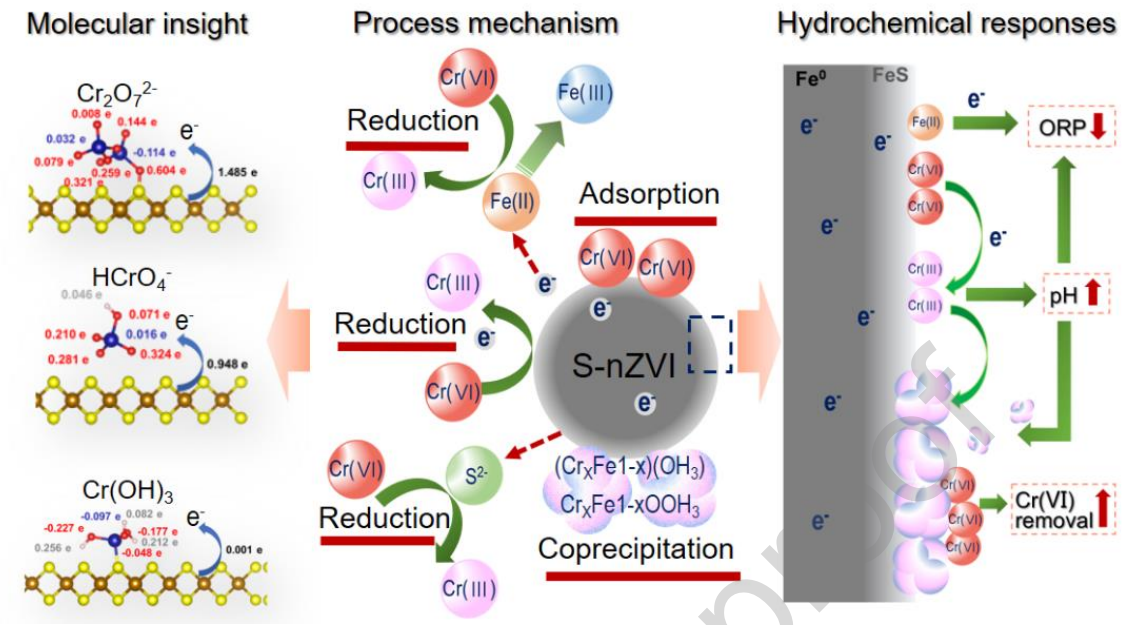

Highlights

- S-nZVI exhibits a desirable removal capacity and remediation efficiency of Cr(VI)
- Cr(VI) reduction pathway involves multi-step reaction with decreasing free energy
- Cr(VI) removed by S-nZVI encompasses adsorption, reduction and coprecipitation
- Cr(VI) removal leads to obviously concurrent pH increase and ORP decrease
- This study provides evidence-based insights into Cr(VI) remediation using S-nZVI